

Boundary treatment algorithms for meshfree RANS turbulence modeling

Mohan Padmanabha^{1,2*}, Jörg Kuhnert¹, Nicolas R. Gauger², Pratik Suchde^{1,3}

¹ Fraunhofer ITWM, Department "Grid-Free Methods", Division "Processes and Materials",
Fraunhofer-Platz 1, Kaiserslautern, 67663, Germany

²Chair for Scientific Computing, RPTU University Kaiserslautern-Landau, Paul-Ehrlich-Strasse 34,
Kaiserslautern, 67663, Germany

³ Faculty of Science, Technology and Medicine, University of Luxembourg, Luxembourg

SUMMARY

In this paper, we propose improved wall-treatment strategies for meshfree methods applied to turbulent flows. The goal is to improve wall-function handling in simulations of high-Reynolds-number turbulent flows, and to better understand the performance of first-order turbulence models when used with meshfree methods. While wall-function techniques are well established for mesh-based methods, their inclusion in meshfree methods faces unique challenges that have not been fully explored. The main difficulties arise from the lack of connectivity between points and from point movement in Lagrangian frameworks, which can complicate consistent wall treatment. To address these issues, we explore three wall-treatment techniques. We highlight the drawbacks of the standard closest neighbor approach, which is commonly used with mesh-based methods. We then introduce two novel approaches: the nearest-band neighbor method and the shifted boundary method. The former applies the wall function to all interior points within a certain distance from the wall, which helps maintain uniform point selection. In the shifted boundary method, boundary points are virtually moved a fixed distance toward the interior, keeping wall-normal distances consistent without extra point selection steps. We evaluate these methods using first-order turbulence closures: Spalart–Allmaras, $k - \varepsilon$, and $k - \omega$. These methods are tested numerically on 1D Couette flow, turbulent flow over a flat plate, and flow around a NACA 0012 airfoil in 3D. The results show that both novel methods outperform the closest neighbor approach. The shifted boundary method achieves higher accuracy, but is more computationally expensive than the nearest-band neighbor method. However, by using smaller shift distances, we can achieve lower y^+ values with the same resolution, which improves efficiency, especially for complex applications. All turbulence models work well with the shifted boundary method, with only minor differences between them. In contrast, the nearest-band method shows variation in the behavior of the turbulence models, where the Spalart–Allmaras model yields better results, especially further downstream along the plate. This work establishes a robust foundation for simulating wall-bounded turbulent flows at high Reynolds numbers using meshfree collocation methods.

KEY WORDS: Wall function; GFDM; Lagrangian framework; CFD; Boundary treatment; Meshfree collocation

1. INTRODUCTION

When simulating turbulent flows close to walls, there is always a trade-off between accuracy and computational cost. Detailed approaches like Direct Numerical Simulation (DNS) or Large Eddy Simulation (LES) can capture all or most turbulence scales, but they are far too computationally demanding for most engineering applications. A more practical alternative is the Reynolds-Averaged Navier–Stokes (RANS) method, which, when combined with suitable turbulence models, offers a good balance between cost and accuracy. To handle the complexity

*Correspondence to: E-mail: mohan.padmanabha@itwm.fraunhofer.de, pratik.suchde@gmail.com

near walls and avoid resolving the boundary layer directly, traditional wall functions are often used in mesh-based methods [30]. These functions help bridge the gap between the unresolved boundary layer and the rest of the flow by relating the wall shear stress to the velocity at the first computational cell or point away from the wall [22].

Conventional CFD methods rely on structured or unstructured meshes to discretize the computational domain. However, generating high-quality meshes for complex geometries can be time-consuming and prone to errors. Managing moving boundaries, especially in Lagrangian simulations, is particularly challenging as it often requires frequent remeshing, which can affect both the accuracy and efficiency of the simulation [27].

Meshfree methods have emerged as an attractive alternative to conventional mesh-based approaches. Instead of fixed grids, these approaches use scattered points with no topological connection to discretize the computational domain [5, 39, 9]. The point cloud-based approach enables automatic generation and adaptation of the domain discretization [46]. The Lagrangian point cloud approach allows dynamic changes in the domain to be captured naturally [49]. Meshfree methods provide distinct advantages over conventional mesh-based approaches, particularly when dealing with free surface flows and multiphase phenomena. Meshfree methods can handle large deformations and complex interfaces dynamically without the requirement of mesh regeneration [40, 36, 39]. Ongoing research continues to enhance meshfree formulations, including improved strategies for velocity-pressure coupling [31]. Recent advancements in meshfree methodologies have allowed diverse multi-physics applications, including free surface interfacial flows [16], multiphase flows [19], cavitation prediction [29], and fluid-structure interaction [57].

Significant progress has been made in meshfree methods to incorporate turbulent flow models. However, most work remains restricted to low Reynolds number regimes [55]. Recent developments have demonstrated LES implementations using meshfree methods with appropriate filtering techniques [32, 2, 34, 1]. However, the high computational costs of these approaches often limit their practical feasibility for high-Reynolds-number flows.

A critical research gap exists in simulating high-Reynolds-number turbulent flows with meshfree methods, with only a limited number of studies attempting to address this challenge [37, 38, 4]. In particular, the main limitation lies in boundary layer treatment and wall function implementation. Similar challenges in boundary treatment have been observed in other non-conforming methods, where improper handling can lead to excessive diffusion near walls [45]. This challenge arises from the fundamental differences between meshfree and mesh-based discretization approaches. While traditional mesh-based methods provide a well-defined wall-adjacent cell or element, meshfree methods require new strategies for identifying wall-adjacent points on which boundary conditions and wall functions can be enforced. In this paper, we address this critical gap in wall boundary treatment for meshfree simulations of turbulent flows, particularly at high Reynolds numbers. Our study also examines the influence of different turbulence models when combined with various wall-treatment methods.

Our main goal is to design, implement, and validate novel wall-treatment methodologies specifically tailored for meshfree collocation approaches within a Lagrangian URANS framework. This study examines three distinct methods for wall function implementation: (i) The first is a closest neighbor approach, which serves as the baseline method for selecting wall-adjacent points. This provides the closest analogy to how wall functions are handled in mesh-based methods. (ii) The second is a novel nearest band neighbor method, designed to select a band of interior neighbors based on their distance from the wall. (iii) The third is a novel shifted boundary method, which virtually shifts the boundary points to a specified distance from the wall. These three boundary treatments are evaluated and compared using the Spalart–Allmaras, $k - \varepsilon$, and $k - \omega$ turbulence models. Validation is performed using established benchmark cases, including flow over a flat plate and flow around a wing with a NACA 0012 airfoil.

All the methods presented in this paper are implemented within the in-house MESHFREE commercial code [15], which is based on the Generalized Finite Difference Method (GFDM).

The meshless GFDM approach considered here uses scattered, non-uniformly distributed point clouds without any background mesh structure. All simulations, except for the 1D Couette flow case, are performed in 3D, making the methods suitable for a wide range of industrial applications.

The remainder of this paper is organized as follows: Section 2 presents the preliminary theoretical background on the Generalized Finite Difference Method (GFDM), flow governing equations, turbulence models, and traditional wall functions. Section 3 explains the implementation of the three wall-treatment methods, including the novel nearest band neighbor method and the shifted boundary method. Section 4 describes the validation test cases and presents results, comparing the performance of the different wall-treatment methods across various turbulence models. Finally, Section 5 presents the conclusions drawn from this research.

2. PRELIMINARIES

In computational fluid dynamics, the momentum equation is a fundamental principle for describing fluid motion. This paper focuses on the Reynolds-Averaged Navier–Stokes (RANS) equations, which utilize turbulence models based on the eddy viscosity concept to represent turbulent flow behavior. This section discusses two modeling techniques. Low Reynolds number models effectively resolve the dynamics within the viscous sub-layer of the boundary layer, but are computationally demanding. Conversely, high Reynolds number models use wall functions to link the near-wall region with the outer flow, enabling coarser discretization. This approach reduces computational costs while maintaining accuracy in predictions of turbulent boundary layers, which is the main focus of this paper. Additionally, the Generalized Finite Difference Method (GFDM) offers a flexible framework for discretizing the governing equations, including the momentum equation, without the constraints of structured mesh generation. This flexibility facilitates the effective analysis of complex geometries and flow conditions. These aspects will be explored below.

2.1. GFDM discretization

The simulations and analyses this work are carried out using the Lagrangian mesh-free method based on the Generalized Finite Difference Method (GFDM) [26]. The simulation domain is decomposed into N numerical points (also referred to as particles), which include points in the interior and on the boundary of the domain. Point placement is based on the advancing front technique [28, 47]. Point density (or refinement) depends on a smoothing function called the resolution h . Points are scattered throughout the domain, and the density of these points is determined by three parameters: r_{\min} , h , and r_{\max} . To avoid point clustering, no two points are allowed within a distance of $r_{\min}h$ from each other. Furthermore, it is ensured that there is at least one point within a sphere of radius $r_{\max}h$. We refer to [49, 47] for details on how these inter-point distances are enforced.

GFDM is a generalized finite difference approach, where the derivative of a function f at a point i is defined as a linear combination of function values at neighboring points [52, 18] :

$$\partial^* f(\vec{x}_i) \approx \tilde{\partial}_i^* f = \sum_{j \in S_i} c_{ij}^* f_j .$$

Here i is the index of the point where the derivative is being computed, and j is the index of neighboring points of point i . Here, '*' represents the differential operator being applied, such as x, y, Δ . The symbol ∂^* denotes the continuous derivative and $\tilde{\partial}^*$ represents the discrete derivative at i . The stencil coefficients c_{ij}^* are computed using the weighted least squares approximation [18].

2.2. Navier–Stokes equation

Consider a fluid flow governed by the conservation equations of mass and momentum:

$$\frac{\partial \rho \vec{u}^*}{\partial t} + \nabla \cdot (\rho \vec{u}^*) = 0, \quad (1)$$

$$\frac{\partial \rho \vec{u}^*}{\partial t} + \nabla \cdot (\rho \vec{u}^* \otimes \vec{u}^*) = -\nabla p + \nabla \cdot \boldsymbol{\sigma} + \vec{g}. \quad (2)$$

Here, \vec{u}^* is the instantaneous velocity, p is the pressure, \vec{g} represents external forces, and $\boldsymbol{\sigma}$ is the stress tensor, defined by:

$$\boldsymbol{\sigma} = \lambda (\nabla \cdot \vec{u}^*) \delta_{ij} + 2\nu \rho \mathbf{S}^*, \quad \text{where } \mathbf{S}^* = \frac{1}{2} (\nabla \vec{u}^* + \nabla \vec{u}^{*T}). \quad (3)$$

Here, λ is the volume viscosity, and ν is the kinematic viscosity. The strain tensor \mathbf{S}^* is computed using the velocity \vec{u}^* .

The instantaneous velocity \vec{u}^* can be decomposed into mean velocity \vec{U} and fluctuating velocity \vec{u} as $\vec{u}^* = \vec{U} + \vec{u}$. By applying Reynolds decomposition and averaging the quantities, we derive the Reynolds-Averaged Navier–Stokes (RANS) equation:

$$\frac{D\vec{U}}{Dt} = -\frac{1}{\rho} \nabla p + \nu \nabla^2 \vec{U} - \nabla \cdot \overline{\vec{u}\vec{u}^T} + \vec{g}. \quad (4)$$

Here, $\frac{D}{Dt}$ is the total derivative, given by $\frac{D}{Dt} = \frac{\partial}{\partial t} + \vec{U} \cdot \nabla$. The averaged components are denoted by $\overline{\cdot}$, when performed over the decomposed Navier–Stokes equations, gives rise to the Reynolds stress tensor $\overline{\vec{u}\vec{u}^T}$, which introduces the closure problem. To address this closure problem, Boussinesq's eddy viscosity assumption [6] is used, where momentum transfer from the turbulent eddies is modeled using eddy viscosity:

$$\overline{\vec{u}\vec{u}^T} = 2\nu_t \mathbf{S} + \frac{2}{3} k \delta_{ij}. \quad (5)$$

Here, ν_t is the turbulent viscosity, which can be obtained using different methods such as algebraic model [41] or first-order turbulence models [56, 3, 10]. \mathbf{S} is the strain tensor computed using the mean velocity \vec{U} , and k is the kinetic energy.

2.3. Turbulence models

Using the eddy viscosity model, Eq. (5), the RANS equation can be closed. However, the turbulent viscosity ν_t must be computed. In this paper, we consider three first-order eddy viscosity models: the one-equation Spalart–Allmaras (SA) turbulence model and the two-equation $k - \varepsilon$ and $k - \omega$ turbulence models, which will be used to compute turbulent viscosity.

2.3.1. Turbulence model Spalart–Allmaras

The Spalart–Allmaras model (SA) uses one transport equation, for $\tilde{\nu}$, which is then used to compute the turbulent viscosity ν_t . Many variations of the original SA model [44] have been proposed. Here, we consider the model without the transition term [3], given by:

$$\frac{D\tilde{\nu}}{Dt} = C_{b1} \tilde{S} \tilde{\nu} - (C_{w1} f_w) \left(\frac{\tilde{\nu}}{d} \right)^2 + \frac{1}{\sigma} \nabla \cdot ((\nu + \tilde{\nu}) \nabla \tilde{\nu}) + \frac{C_{b2}}{\sigma} (\nabla \tilde{\nu})^2. \quad (6)$$

Here, \tilde{S} is computed using the rotation and strain tensors, C_{b1} , C_{w1} , σ , and C_{b2} are the model constants, and f_w is a coefficient that depends on \tilde{S} and the distance from the nearest boundary d . The turbulent viscosity ν_t required for the eddy viscosity model is obtained from:

$$\nu_t = \tilde{\nu} f_{v1}. \quad (7)$$

Here, f_{v1} is a scalar factor used to scale the values of $\tilde{\nu}$, and the value of $\tilde{\nu}$ approaches 0 at the wall.

2.3.2. Turbulence model $k - \varepsilon$

Originally proposed by Chien [10], the $k - \varepsilon$ turbulence model is similar to the SA model, but with two transport equations: one each for the kinetic energy k and dissipation rate ε :

$$\frac{Dk}{Dt} = P - \varepsilon + \nabla \cdot \left(\rho \left(\nu + \frac{\nu_t}{\sigma_k} \right) \nabla k \right), \quad (8)$$

$$\frac{D\varepsilon}{Dt} = C_{\varepsilon 1} f_1 \frac{\varepsilon}{k} P - C_{\varepsilon 2} f_2 \frac{\varepsilon^2}{k} + \nabla \cdot \left(\rho \left(\nu + \frac{\nu_t}{\sigma_\varepsilon} \right) \nabla \varepsilon \right). \quad (9)$$

Here, P is the production term computed using $P = \rho \nu_t S^2$. The model-based coefficients are σ_k , $C_{\varepsilon 1}$, $C_{\varepsilon 2}$, f_2 , and σ_ε . The turbulent viscosity ν_t is obtained from the kinetic energy k and dissipation rate ε :

$$\nu_t = C_\mu \frac{k^2}{\varepsilon}. \quad (10)$$

The values of k and ε are scaled using the coefficient $C_\mu = 0.09$ [10]. The kinetic energy k and the dissipation rate ε approach 0 at the wall.

2.3.3. Turbulence model $k - \omega$

The second two-equation eddy viscosity model considered here is $k - \omega$. Several variations of the original model have been proposed. The model that we have considered here is based on [56]. The transport equations for the kinetic energy k and specific dissipation rate ω are given by:

$$\frac{Dk}{Dt} = P - \beta^* \omega k + \nabla \cdot \left(\rho \left(\nu + \sigma_k \frac{k}{\omega} \right) \nabla k \right), \quad (11)$$

$$\frac{D\omega}{Dt} = \frac{\gamma \omega}{k} P - \beta \omega^2 + \nabla \cdot \left(\rho \left(\nu + \sigma_\omega \frac{k}{\omega} \right) \nabla \omega \right) + \frac{\sigma_d}{\omega} \nabla k \cdot \nabla \omega. \quad (12)$$

Here, similar to the $k - \varepsilon$ model, P is the production term; and β^* , β , σ_k , σ_ω , and σ_d are the model coefficients. The turbulent viscosity is obtained from k and ω :

$$\nu_t = \frac{k}{\omega}. \quad (13)$$

At the wall, the kinetic energy is $k_w = 0$ as in the $k - \varepsilon$ model. The specific dissipation rate ω tends to infinity as it approaches the wall. This boundary condition cannot be specified for numerical implementation; hence, the proposed boundary condition [56] is:

$$\omega_w = \frac{6\nu_w}{\beta_0 d^2}. \quad (14)$$

Here, $\beta_0 = 0.0708$; ν_w is the viscosity at the wall, and d is the distance between the wall and the closest interior point.

2.4. Wall-bounded turbulent flow and wall functions

Many industrial applications involve wall-bounded flow, where turbulence generated by the wall has a significant influence on the flow profile. The velocity variations from the no-slip boundary to the free-stream flow are large, resulting in high velocity gradients, especially close to the wall. To resolve this flow numerically, a finer discretization is required close to the wall. This method of resolving the boundary layer with fine discretization is known as the low Reynolds number method. While the boundary layer can be captured accurately with this approach, the finer discretization is computationally expensive. To avoid high computation costs and to use coarser discretization close to the boundary, wall corrections are performed to determine approximate values using the laws of the wall. This method is known as the high Reynolds number model.

2.4.1. The laws of the wall

The flow close to the no-slip wall in the boundary layer can be categorized into three different layers based on the behavior of the flow [41, 54], known as the laws of the wall. The type of layer is determined based on the dimensionless wall-normal coordinate y^+ and the dimensionless wall velocity U^+ . These quantities, y^+ and U^+ are computed using the friction velocity U_τ , which is in turn computed using the wall shear stress τ_w .

$$y^+ = \frac{y_p U_\tau}{\nu} \quad \text{and} \quad U^+ = \frac{U_p}{U_\tau} \quad \text{where} \quad U_\tau = \sqrt{\frac{\tau_w}{\rho_w}}. \quad (15)$$

Here, ν and ρ_w are the kinematic viscosity and the density of the fluid respectively, and U_p and y_p represent the velocity and the distance from the wall at the location of interest in the fluid domain.

The three layers comprising the wall region are the viscous sub-layer, buffer layer, and inertial sub-layer (or log layer). The viscous sub-layer ranges from $0 < y^+ < 5$, where the turbulent effects are negligible compared to the viscous effects. The viscous sub-layer follows the relation $U^+ = y^+$. The buffer layer ranges from $5 < y^+ < 30$, where turbulent and viscous effects both vary significantly, making it difficult to derive a generalized model for turbulence. The inertial sub-layer, or log layer, ranges from $30 < y^+$ to the end of the boundary layer. In the log layer, the turbulent effects are dominant, and the viscous effects are negligible. The asymptotic relation of y^+ and U^+ exhibits logarithmic behavior:

$$U^+ = \frac{1}{\kappa} \ln(Ey^+). \quad (16)$$

where $\kappa = 0.41$ is the von Kármán constant, and $E = 9.8$. Due to the logarithmic relation, additional modifications (wall functions) are required to capture the appropriate behavior of the flow near the wall.

3. METHODOLOGY

Turbulence behavior in 3D simulations using meshfree collocation methods has received limited attention. The aim of this paper is to examine the behavior of first-order turbulence models, Spalart–Allmaras, $k - \varepsilon$, and $k - \omega$ in the mesh-free collocation architecture, especially with the aspect of high Reynolds number models, with the implementation of wall functions.

Wall functions and their implementation in mesh-based methods are well established, where the modification to the equation is carried out for the first internal points/cells/elements attached to the boundary. Selecting these points is straightforward, and wall function application has been studied extensively [25, 13, 7]. In meshfree methods, the location where the wall function should be applied is not obvious. In this work, we propose and analyze three approaches to applying the wall function.

In each approach, for each boundary point, either a single interior point or a set of interior points is selected for wall function application. Wall function modifications are based on the distance from the first interior point to the wall. The computed corrections are then incorporated into the momentum and turbulence equations.

To determine the velocity correction, the respective y^+ and U^+ must be computed at the first interior point's distance from the wall. To compute y^+ at that location, U_τ is required, which is also unknown. To obtain y^+ , we iterate the following equations until convergence is achieved.

$$U_\tau = \frac{U_p \kappa}{\ln(Ey_p^+)} \quad \text{where } y_p^+ \text{ is computed using: } y_p^+ = \frac{y_p U_\tau}{\nu}. \quad (17)$$

Here, y_p and U_p represent the distance and the velocity magnitude at the first interior point p from the wall. The constants are $E = 9.8$ and $\kappa = 0.41$, and ν is the kinematic viscosity of the fluid. y_p^+ is the y^+ at the location p . If the turbulent kinetic energy k is available, we initialize

U_τ using $U_\tau = C_\mu^{1/4} \sqrt{k_p}$ and iterate until convergence is achieved. Based on the obtained y_p^+ value, the effective wall shear stress τ_w is computed using:

$$\tau_w = \frac{\rho U_\tau U_p \kappa}{\ln(Ey^+)} . \quad (18)$$

Here, the shear stress τ_w is added as a source term to the momentum equation. The correction can also be made by computing the effective wall viscosity ν_w using:

$$\nu_w = \nu \left(\frac{y^+ \kappa}{\ln(Ey^+)} - 1 \right) . \quad (19)$$

Wall functions must be adopted based on where the first interior point next to the boundary in the turbulent boundary layer is located. If the point lies in the viscous layer, no wall function is used; if the point lies in the log layer, the wall function defined above is used. If the point lies in the buffer layer, there is no single solution available; hence, different strategies can be applied [21] [25]. The standard method [25] is to use a switching strategy where points up to the midpoint of the buffer region are treated with the viscous law, requiring no wall function. If the point p lies above the midpoint of the buffer layer, then the log layer function is used. Another strategy is the blending function [21], which provides a smooth transition from the viscous to the log region. In this paper, we use Reichardt's wall function [42]:

$$U^+ = \frac{1}{\kappa} \ln(1 + \kappa y^+) + 7.8 \left(1 - \exp \left(-\frac{y^+}{11} \right) - \frac{y^+}{11} \exp \left(-\frac{y^+}{3} \right) \right) . \quad (20)$$

Reichardt's wall function smoothly blends all three regions of the wall law into a single continuous expression, eliminating the need to switch between different equations.

Turbulence models wall treatment

Along with the momentum equation, the turbulence models must also be modified. Wall functions have been studied extensively, especially in mesh-based methods [54] [22].

The wall function for Spalart–Allmaras is straightforward, as the modifications apply only to the momentum equation and not to the Spalart–Allmaras transport equation. The modification to the momentum equation follows the approach shown in the section 2.4.1 based on the location of the first interior point p .

With two-equation turbulence models $k - \omega$ and $k - \varepsilon$, modifications are applied to k_p and ω_p or ε_p at interior points p close to the boundary selected for applying wall function.

The standard wall function

For the standard wall function [25], the modification is carried out by setting the value of the turbulent kinetic energy k_p directly on the first interior point p based on the computed shear velocity U_τ and the coefficient C_μ . The value of U_τ is computed based on the location of the first interior point from the boundary p as:

$$k_p = \frac{U_\tau^2}{\sqrt{C_\mu}} . \quad (21)$$

The values of ω_p and ε_p at the first interior point are modified based on the value of k_p . The modifications performed on the equations of ω_p and ε_p are:

$$\omega_p = \frac{\sqrt{k_p}}{C_\mu^{1/4} \kappa y_p} \quad \text{and} \quad \varepsilon_p = \frac{C_\mu^{3/4} k_p^{3/2}}{\kappa y_p} . \quad (22)$$

Where $C_\mu = 0.09$, $\kappa = 0.41$, and the values of k_p and y_p at the first interior point p are used.

The Launder–Spalding wall function

The other wall function methodology considered is the Launder–Spalding wall function [25]. Here, the value of k_p is not directly changed at the first interior point, as in the standard wall-function method. Instead, the production term in the transport equation for k_p is modified to obtain the production-dissipation relation as:

$$P_{k_p} = U_\tau^2 \frac{U_\tau}{\kappa y_p}. \quad (23)$$

Where P_{k_p} is the production term in the transport equation for turbulent kinetic energy k_p . For ω_p or ε_p , the values are directly computed based on the value of k_p at the first interior point, similar to the standard wall function.

Implementing wall functions in meshfree methods

In this paper, we propose three methods to incorporate wall functions and boundary treatment for meshfree collocation methods. The three methods differ in how the first interior points from the boundary are selected to apply the wall function.

Without sufficient resolution to resolve the boundary layer, wall functions must be applied for the velocity correction at the first interior point(s) adjacent to the wall. To enforce wall function corrections, we must select the first interior point(s). Due to the presence of scattered points in meshfree collocation methods, the choice of the first interior point is ambiguous, as there is no topology or any direct connection to the boundary. A second challenge is that the points move with the flow (in a Lagrangian sense); hence, point selection must be performed at each time step. We consider the closest neighbor method and two novel methods proposed in this paper to address the problems in meshfree methods. The first method adapts the classical mesh-based approach to the mesh-free situation by choosing the closest neighbor to the boundary point. The two novel methods discussed are the nearest-band neighbor method and the shifted-boundary method. Each method is evaluated with meshfree collocation using the turbulence models discussed earlier.

Remark: In several figures below, the distance between boundary points and the closest interior points is exaggerated for ease of visualization.

3.1. Closest neighbor (CN) method

The first method is based on the approach used in mesh-based methods [54]. Here, for each boundary point, we apply the wall function to its closest interior point, see Figure 1. First, we flag the boundaries where the wall functions are required. For each boundary point on the flagged boundaries, we select the closest interior point for wall function application. We repeat this process at each time step. Since the points move with the flow in a Lagrangian sense, the closest neighbor points must be recomputed at every time step. For the boundary points used to select interior points for the wall function, we change their boundary condition from a no-slip condition to a Neumann (zero-gradient) condition.

Since the wall function is applied to a single closest neighbor for each boundary point, we refer to this method as the closest neighbor (CN) method. The implementation of the CN method within a Lagrangian meshfree solver is shown in Algorithm 1.

This method has several drawbacks. In certain flow scenarios, such as downdrafts or shear, some interior points may move closer to the boundary points than other neighboring interior points. As illustrated in Figure 2, a single interior point might be the closest interior neighbor of multiple boundary points. At the same time, other interior points near the boundary might not be the closest interior point for any boundary point. Thus, the wall function is applied only to the single closest point, ignoring the other neighboring points. This leads to non-uniform application of the wall function near the boundary. The lack of uniform wall function coverage leads to incorrect solutions during gradient or Laplace operations. Because points move in a Lagrangian sense, such gaps might propagate or appear even when there was no gap in the previous time step. This situation is amplified in 3D simulations and for curved

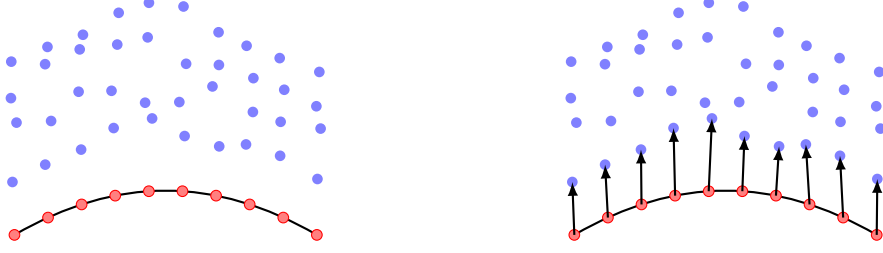


Figure 1. Illustration of the closest neighbor selection method in 2D, Red points are boundary points, blue points are interior points, and the solid line is the boundary wall. The arrow represents the identification of the closest interior neighbor point for each boundary point.

Algorithm 1 Algorithm for Closest neighbor(CN) method

```

1: while time step loop do
2:   Lagrangian point cloud movement                               ▷ see [51]
3:   Update neighbor tree
4:   Add/delete points to prevent holes/clustering                ▷ section 2.1
5:   For each wall point, flag the closest interior neighbor point ▷ section 3.1
6:   for all  $i \in$  Point cloud do
7:     Setup of momentum equation for velocity
8:     if  $i$  is Flagged CN then
9:       Impose the computed wall stress as source term to momentum equation      ▷
   equation (18)
10:    else if  $i$  is wall points then
11:      Set appropriate boundary condition
12:    end if
13:  end for
14:  Solve mass and momentum conservation equations
15:  for all  $i \in$  Point cloud do
16:    Setup of turbulence equation {SA,  $k - \varepsilon$  or  $k - \omega$ }                  ▷ section 2.3
17:    if  $i$  is Flagged CN then
18:      Update turbulent quantities based on wall function                      ▷ section 3
19:    else if  $i$  is wall points then
20:      Set appropriate boundary condition
21:    end if
22:  end for
23:  Solve turbulence equations and update turbulent viscosity  $\nu_t$            ▷ section 2.3
24:  Post-processing calculations
25: end while

```

boundaries. This drawback necessitates the development of alternative approaches to apply the wall functions, which motivates the next two approaches proposed.

3.2. Nearest-band neighbor (NBN) method

To overcome the non-uniform wall function application, we propose the application of the wall function to not just the closest interior neighbor of a boundary point but also to all interior neighbors within a specified distance δh , as shown in Figure 3. Here, h is the resolution, and $r_{\min}h < \delta h < h$, where r_{\min} is the minimum separation factor (as a fraction of h) where the points are deleted for being too close to the boundary (see Section 2.1). We refer to this approach as the nearest-band neighbor method (NBN), since interior points are selected within

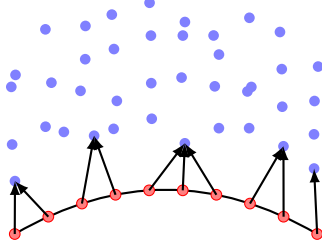


Figure 2. Closest neighbor method. Illustration of non-uniform coverage of the selection of the closest neighbor points in the interior points. Each boundary point (red dot) looks for the closest neighbor interior point (blue dot), leading to regions where there are no interior points selected, causing numerical instabilities.

a band close to the boundary. The appropriate distance δh by which the points need to be selected will be studied in Section 4 for uniform point selection and numerical accuracy. The boundary points used to select interior points for the wall function are given a Neumann (zero-gradient) boundary condition similar to that of the closest neighbor method.

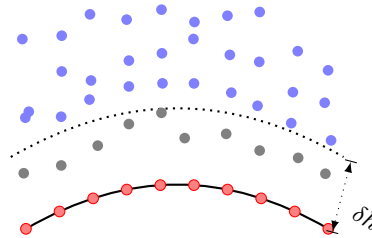


Figure 3. Nearest-band neighbor method. Selection of neighbor interior points based on specified distance δh . Due to non-uniformity of the point distribution, the selection of interior points (gray dot) for application of wall functions is made based on the distance δh (shown by dotted line) to the boundary, allowing for uniform selection of points. Other interior points are marked with blue dots.

As with the CN method described above, in the NBN method, we must select of nearby points at each time step due to the Lagrangian movement of points. The implementation of the NBN method within a Lagrangian meshfree solver is shown in Algorithm 2.

3.3. Shifted-boundary (SB) method

In both methods above, for each boundary point, there is an explicit selection process to choose the interior points with reference to the boundary point, where the wall function will be applied. We now propose another novel approach for applying the wall function that avoids this selection process for the interior points altogether. In this method, we virtually shift the boundary points by a distance αh in the normal direction towards the interior. These shifted points are treated as interior points, and wall functions are applied to them. Since these boundary points are treated as virtual shifted points while the physical points remain on the boundary, no additional selection process for interior points is required. This process of virtually shifting the boundary points in the normal direction towards the interior of the domain is illustrated in the Figure 4. We refer to this approach as the shifted-boundary (SB) approach.

Since the virtual shifted points are treated as interior points, they move with the flow when the velocity is non-zero. The points act as Lagrangian points and move with the flow. To

Algorithm 2 Algorithm for Nearest-Band Neighbor(NBN) method

```

1: while time step loop do
2:   Lagrangian point cloud movement                                ▷ see [51]
3:   Update neighbor tree
4:   Add/delete points to prevent holes/clustering                  ▷ section 2.1
5:   Flag all interior points  $< \delta h$  from wall points            ▷ section 3.2
6:   for all  $i \in$  Point cloud do
7:     Setup of momentum equation for velocity
8:     if  $i$  is Flagged NBN then
9:       Impose the computed wall stress as source term to momentum equation      ▷
   equation (18)
10:    else if  $i$  is wall points then
11:      Set appropriate boundary condition
12:    end if
13:  end for
14:  Solve mass and momentum conservation equations
15:  for all  $i \in$  Point cloud do
16:    Setup of turbulence equation {SA,  $k - \varepsilon$  or  $k - \omega$ }                  ▷ section 2.3
17:    if  $i$  is Flagged NBN then
18:      Update turbulent quantities based on wall function                  ▷ section 3
19:    else if  $i$  is wall points then
20:      Set appropriate boundary condition
21:    end if
22:  end for
23:  Solve turbulence equations and update turbulent viscosity  $\nu_t$           ▷ section 2.3
24:  Post-processing calculations
25: end while

```

maintain the shifted distance at αh for the virtually shifted points, we treat these points in a semi-Lagrangian manner, allowing movement only in the tangential direction while fixing them in the normal direction. These restrictions require special treatment so the virtual points behave as Lagrangian points in the tangential direction and Eulerian in the normal direction to the boundary plane. This leads to the modification of the gradient and Laplace approximations in the normal direction for the momentum and turbulence equations. We compute this using the classical finite difference approach based on the shift distance. Computing the diffusion operator with the classical finite difference method requires additional information on the interior side of the virtual shifted point. To provide this information, we introduce an additional virtual layer of thickness βh solely for approximating the values needed for the diffusion operator. The approximation of the tangential component requires no modification, since the points are Lagrangian in the tangential direction; the gradient and Laplace approximations are computed using the GFDM method. The differential operator modification is only carried out for the boundary points, which are virtually shifted. Other points in the domain require no modification.

While all earlier figures illustrate the 2D scenario for ease of visualization, the formulation below, and the numerical results in Section 4, consider the general 3D scenario. For the virtually shifted points, while solving the flow and turbulence equations, the gradient approximation is split into normal and tangential components:

$$\nabla f = (\nabla f \cdot \vec{n})\vec{n} + \nabla_T f, \quad (24)$$

where f is a variable for which the gradient needs to be computed, \vec{n} is the unit normal vector. The normal component of the gradient is $(\nabla f \cdot \vec{n})\vec{n}$. The tangential component of the gradient, denoted by $\nabla_T f$, is computed using GFDM. For GFDM computation of the

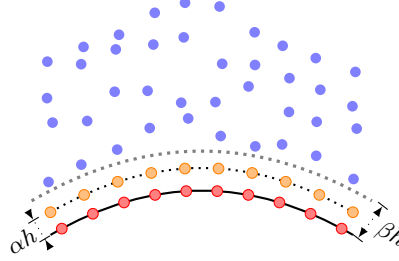


Figure 4. Illustration of the shifted-boundary method in 2D with additional shifted points. The boundary points (red dots) are virtually shifted (orange dots) to a distance of αh and are treated as interior points but fixed at a height of αh (dotted line) in the normal direction during the simulation.

The momentum thickness approximation is carried out at the height of βh (gray dotted line).

tangential differential operator, we restrict neighborhood selection to the boundary points and calculate the gradient in the tangential plane [48].

For the computation of the gradient in the normal direction, the standard finite difference scheme is used:

$$(\nabla f \cdot \vec{n}) \approx \frac{f_{\text{shifted}} - f_{\text{boundary}}}{\alpha h}, \quad (25)$$

where f_{shifted} is the value at the shifted point, f_{boundary} is the value at the boundary point, and αh is the shift distance. Thus, the gradient computation at the shifted points is given by:

$$\nabla f = \nabla_T f + \left(\frac{f_{\text{shifted}} - f_{\text{boundary}}}{\alpha h} \cdot \vec{n} \right) \vec{n}. \quad (26)$$

We compute the Laplace operator similarly by splitting it into the normal and tangential components $\Delta f = \Delta_n f + \Delta_T f$. Where $\Delta_n f$ is the normal component and $\Delta_T f$ is the tangential component. The computation of the tangential part is carried out using GFDM by considering only boundary points, similar to the gradient operator. In the normal direction, the computation is performed using a simple finite difference scheme as:

$$\Delta_n f = \left(\frac{f_{\text{momentum}} - f_{\text{shifted}}}{\beta h - \alpha h} - \frac{f_{\text{shifted}} - f_{\text{boundary}}}{\alpha h} \right) \frac{2}{\beta h}. \quad (27)$$

Here $\Delta_n f$ represents the Laplacian in the normal direction, αh is the shift distance, and f_{momentum} is the function value approximated at the height of βh from the boundary location. The approximation of f_{momentum} is carried out using only the interior points, excluding the virtual shifted points and boundary points. The impact of the parameters α and β on numerical accuracy will be presented in Section 4. The implementation of the SB method within a Lagrangian meshfree solver is shown in Algorithm 3.

4. RESULTS

We now investigate the performance of the three proposed boundary treatment methods: the closest neighbor method, the nearest-band neighbor method, and the shifted-boundary method. The boundary treatment methods are evaluated on first-order turbulence models, namely the Spalart–Allmaras (SA), $k - \varepsilon$, and $k - \omega$ models with wall functions. Common validation test cases are chosen such that the results obtained can be readily validated against available data. Initially, we focus on a one-dimensional (1D) scenario involving Couette flow, which provides a straightforward implementation and testing environment. Following this, we examine more complex simulations, including flow over a flat plate and flow around a NACA 0012 airfoil, both analyzed in three dimensions to encompass different potential flow

Algorithm 3 Algorithm for Shifted Boundary(SB) method

```

1: while time step loop do
2:   Lagrangian point cloud movement                                ▷ see [51]
3:   Update neighbor tree
4:   Add/delete points to prevent holes/clustering                  ▷ section 2.1
5:   for all  $i \in$  Point cloud do
6:     Setup of momentum equation for velocity
7:     if  $i$  is wall points then
8:       Virtual shift points  $ah$  in the normal direction
9:       Compute the differential operator in normal and tangential direction for velocity
  ▷ equations (26) (27)
10:      substitute the newly computed differential operators in momentum equation
11:      end if
12:    end for
13:    Solve mass and momentum conservation equations
14:    for all  $i \in$  Point cloud do
15:      Setup of turbulence equation {SA,  $k-\varepsilon$  or  $k-\omega$ }          ▷ section 2.3
16:      if  $i$  is wall points then
17:        Compute the differential operator in normal and tangential direction for
        turbulent quantities                                         ▷ equations (26) (27)
18:        Set up the turbulent equations according to the wall functions    ▷ section 3
19:      end if
20:    end for
21:    Solve turbulence equations and update turbulent viscosity  $\nu_t$           ▷ section 2.3
22:    Post-processing calculations
23: end while

```

scenarios. All the turbulence models and boundary treatment methods introduced above were implemented in the in-house commercial software MESHFREE [15]. The time integration in MESHFREE is performed using the segregated, predictor-corrector approach [8, 11]. Initially, the integration starts with the second-order Lagrangian movement of the points [50]. The velocity predictions are computed using the momentum equations via a first-order implicit scheme. Followed by the projection step from the pressure Poisson equation to ensure mass conservation and to obtain the corrected velocity, followed by a pressure update [52]. The turbulent equations are computed with an implicit time integration scheme. Further details regarding the time integration scheme can be referenced in [14, 20, 23, 35, 52].

4.1. 1D simulation case of Couette flow

The 1D case of Couette flow is selected as the first test case to simplify the governing equations of both the turbulence models and the Navier–Stokes equations by eliminating the convection term and the velocity-pressure coupling. For the computation of differential operators, a classical finite-difference scheme is used. We consider a long channel with a height H (see Figure 5). The bottom plate of the channel remains fixed, while the top plate moves at a constant velocity U_m . Because the motion of the upper plate drives the flow, the velocity variation occurs solely in the normal direction. Since velocity varies only in one direction, a 1D simulation along the height H of the channel is sufficient. We can neglect the convection term. Furthermore, a zero-pressure gradient case is considered.

The simulation parameters are chosen to replicate those from the work of Telbany et al. [53], where channel height $H = 0.066$ m and the top moving wall velocity $U_m = 12.8 \frac{\text{m}}{\text{s}}$. The fluid properties considered are those of air, with a density of 1 kg/m^3 and viscosity of $1.388 \times 10^{-5} \text{ m}^2/\text{s}$, assuming incompressibility. Three turbulence models, SA, $k - \varepsilon$, and $k - \omega$, are implemented, with both the closest neighbor method (In 1D, the closest neighbor method

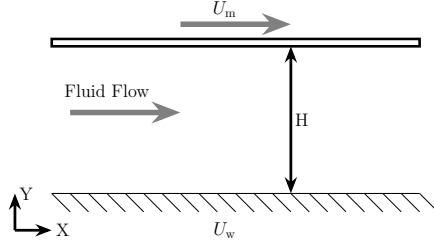


Figure 5. 1D Couette Flow schematic illustrating the configuration with a fixed bottom plate with velocity $U_w = 0 \frac{\text{m}}{\text{s}}$ and a moving top plate. The flow is driven by the top plate U_m , including the height H and the moving wall velocity $U_m = 12.8 \frac{\text{m}}{\text{s}}$. The 1D simulation is carried out along the channel height H .

and the nearest-band neighbor method are identical) and shifted-boundary methods. For the 1D discretization, points are distributed equidistantly with a discretization size dx along the height H .

The results obtained from the closest neighbor method and shifted boundary method are validated against experimental data from [53]. The velocity profiles across different turbulence models are compared to experimental results. The 1D domain is discretized into N equidistant grid points with grid size dx .

The analysis begins with the closest boundary method, which is straightforward to execute. As described in the section 3, the first interior node is selected for applying the wall function. The number of discretization points is fixed to $N = 40$ so that the first interior point lies on the log layer. Both the standard and Launder–Spalding wall function methods [25, 54] are employed for the $k - \varepsilon$ and $k - \omega$ models, and the standard wall function is used for the Spalart–Allmaras model. The simulation is carried out until the residues such as the velocity (U) and turbulent viscosity (ν_t) are lower than 10^{-8} . The initial conditions are fixed based on the moving wall's velocity U_m , with boundary conditions specified as mentioned above.

When comparing the performance of different turbulence models against experimental results, we observe that all the turbulence models follow the velocity profile of the experimental results. This is illustrated in Figure 6. A slight variation can be observed with the turbulence model, especially with the $k - \varepsilon$ model, towards the moving wall, demonstrating that the $k - \omega$ model is slightly more accurate near the wall compared to the $k - \varepsilon$ model [33].

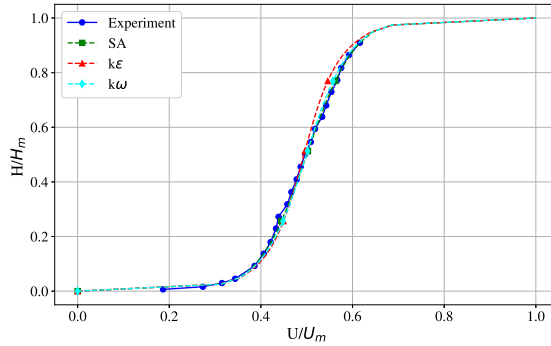


Figure 6. 1D Couette Flow results comparison using the closest neighbor method against experimental results. Velocity profiles show the performance of $k - \omega$ (cyan line), $k - \varepsilon$ (red line), and Spalart–Allmaras (green line) turbulence models against the experimental results (blue line) from [53], particularly near the wall, showcasing the accuracy of the closest neighbor approach.

The simulation setup for the shifted-boundary method is similar to that of the closest neighbor method, with the distinction that the boundary points are shifted from the wall by a

specified distance. Here, the shifted distance αh is set to $0.5dx$, while the momentum boundary thickness βh is $1.0dx$. Various values of αh and βh are tested to evaluate their effects on the simulation results. The number of points for the SB method is reduced to $N = 20$ to make sure that the shifted point lies in the log layer.

The comparison of the velocity profiles of different turbulence models can be seen in Figure 7. The results obtained from the shifted boundary method produce similar results to those of the closest boundary method. We observe that the velocity profile of $k - \varepsilon$ with the SB method matches well with the experimental results, similar to that of the CN method. The minor oscillations observed in the CN method are not observed here. Boundary points are not visible in Figure 7, because we have virtually shifted the boundary points to treat them as interior points at a distance $0.5dx$ from the wall.

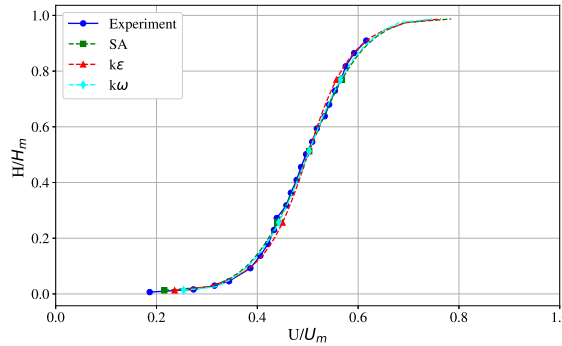


Figure 7. 1D Couette Flow results comparison with the shifted-boundary method. Velocity profiles from the simulation are compared with experimental data, demonstrating the effectiveness of the shifted-boundary treatment.

Both the shifted-boundary and closest neighbor methods yield good agreement with the experimental results. The number of points in the SB method is reduced from $N = 40$ to $N = 20$ to maintain approximately the same y^+ value, but the velocity profiles still match well with experimental results. We also see that the $k - \varepsilon$ turbulence model with the SB method produces less oscillation compared to that of the CN method. As the boundary treatment methods produced promising results with 1D simulation, the next step is to test the method in a 3D environment to assess the behavior of the boundary treatment methods.

4.2. Flow over a flat plate

The next simulation case involves turbulent flow over a flat plate, a widely studied test case in fluid dynamics. This simulation is configured in either 2D or 3D, utilizing symmetry boundary conditions along the sidewalls. The focus of the present work is to adapt the boundary treatment and turbulence model implementation for industrial applications, which predominantly require 3D simulations. Thus, we only consider a 3D geometry here, which can help identify potential challenges or limitations in actual applications. The simulation setup consists of a flat plate of length 2 m placed in a rectangular channel with a height of 1 m (see Figure 8).

A slip boundary condition is enforced for the section preceding the flat plate, measuring 0.33 m, while the flat plate itself is treated as a no-slip boundary. The inlet conditions specify a velocity of 69.4 m/s and a pressure gradient of zero. The fluid properties remain the same as the previous case, using air with incompressible flow, with a density of 1.0 kg/m^3 and viscosity of $1.388 \times 10^{-5} \text{ m}^2/\text{s}$. The simulation continues until a steady state is achieved. The flow behavior at the wall is studied using the skin friction coefficient C_f computed with the help of wall shear stress τ_w ,

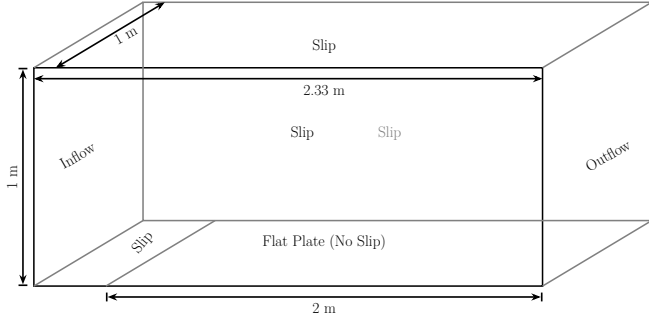


Figure 8. Flow over a flat plate geometry setup, illustrating the dimensions of the rectangular channel and the placement of the flat plate. Includes inlet conditions such as specified velocity and pressure gradient, along with slip and no-slip boundary condition sections.

$$Re_x = \frac{\rho_\infty U_\infty x}{\mu_\infty}, \quad \tau_w = \mu_w \left(\frac{\partial U}{\partial y} \right)_w, \quad C_f = \frac{\tau_w}{\frac{1}{2} \rho_\infty U_\infty^2},$$

where ρ_∞ , U_∞ , μ_∞ are the bulk density, velocity, and viscosity values well above the boundary layer. Here, x represents the distance along the flat plate where the respective values are computed. To compute the wall shear stress τ_w , the wall viscosity μ_w and velocity gradient at the wall $\left(\frac{\partial U}{\partial y} \right)_w$ are used. The computed skin friction coefficient C_f is validated against analytical expressions $C_{f,\text{analytic}} = 0.0592 Re_x^{-1/5}$ [17, 43].

We now evaluate the three proposed boundary treatments for wall function application: (i) the closest-neighbor (CN) method, (ii) the nearest-band neighbor (NBN) method, and (iii) the shifted-boundary method (SB) for the test case of turbulent flow over a smooth, zero-pressure-gradient flat plate. Instantaneous skin-friction $C_f(x)$ data without temporal averaging, extracted along the streamwise direction at the midspan line ($y = 0.5$ m) are validated against the analytical data. Unless stated otherwise, all simulations employ identical parameters, with the $k - \omega$ turbulence model and resolution $h = 0.0035$ m for the CN method and the NBN method. The resolution for the SB method is chosen to be a coarser resolution of $h = 0.005$ m. The resolution is determined via grid-convergence studies; a coarser resolution of $h = 0.005$ m is chosen for the SB method to maintain a similar y^+ value for both NBN method and SB method. Wall-adjacent points are constrained to lie within the logarithmic layer to ensure valid wall function enforcement. The exact y^+ band depends on the local resolution but remains within the log-layer in all cases.

4.2.1. Closest-neighbor (CN) Method Analysis As described in Section 3.1, the closest-neighbor (CN) method selects only the single nearest interior point to each wall point to apply the wall function. This selection isn't uniform along the wall, so some wall points get proper treatment while others do not. Because of this, the wall function is applied unevenly, and the wall resistance is underestimated. As a result, the skin friction C_f extracted along the flat plate (at $y = 0.5$ m) is higher than expected, and the velocities are also higher, see Figure 9. We also observe large instantaneous fluctuations. As a result, the CN method is not used for further simulations.

4.2.2. Nearest-band neighbor (NBN) Method Analysis With the NBN method, instead of selecting only the closest point, we select all interior points within a certain distance δh from the wall (see Section 3.2). Here, we use the selection height δh so that there are always enough points selected near the wall to apply the wall function evenly. This results in a more uniform wall resistance and more accurate simulations. We also observe reduced oscillations when

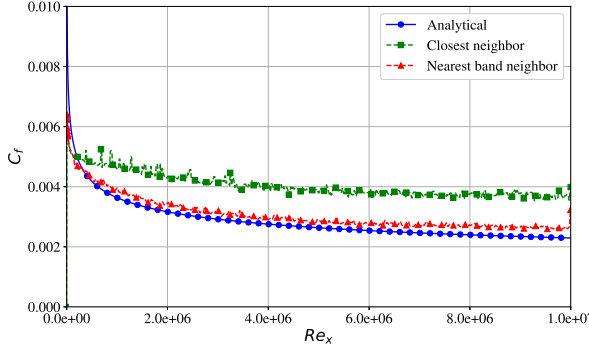


Figure 9. Skin friction coefficient C_f comparison of the closest neighbor (CN) method (green) with the Nearest-band neighbor (NBN) method (red) and the analytical expression (blue). Comparison of C_f shows a large deviation in the prediction of C_f for the CN method due to inadequate points selected to apply the wall function.

compared with the CN method, see Figure 9. The NBN method is now examined further to study the wall function effects, selection height sensitivity, and turbulence model behavior.

We now compare the two strategies of the standard method and Launder–Spalding method discussed in Section 2.4 applied to the wall-adjacent points when enforcing wall functions.

For the zero-pressure-gradient flat-plate case, both methods yield comparable $C_f(x)$ as seen in the Figure 10. We therefore proceed with the Launder–Spalding method in subsequent simulations because it preserves transport consistency for k while utilizing wall-stress information in production.

The next step is to assess the sensitivity of the selection height δh . Selection height plays a crucial role in applying wall functions. If the selection height is inadequate, fewer or no points may be selected to apply the wall function, which will produce the same or worse results as the CN method. If the selection height is large, points outside of the boundary layer will be selected, which is not the correct approach. Hence, the selection height study is crucial to determine the appropriate height that needs to be selected to apply the wall function.

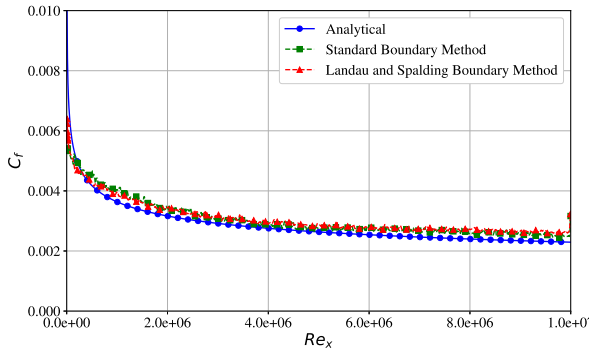


Figure 10. Comparison of Skin friction coefficient C_f for different wall function methods using the NBN method. The plot shows a comparison of the standard wall function (green) and Launder–Spalding wall function (red) against the analytical expression (blue) where we see no large difference between the two wall-function methods.

We consider several values of the parameter δ , namely $\delta h \in \{0.3h, 0.5h, 0.7h, 1.0h\}$. We choose $\delta h > 0.2h$ since $r_{\min}h = 0.2h$, which means that there are no points closer than $0.2h$ to the wall (see Figure 11). Thus, setting $\delta h < 0.2h$ would make the NBN method similar to

the CN method with too few points selected. On the other hand, setting $\delta h > h$ means picking points too far away, beyond the neighborhood of the wall, which would also reduce accuracy.

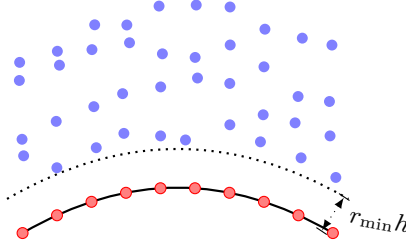


Figure 11. Deletion of points if the points get closer than $r_{\min}h$ even between the wall (red) and fluid points (blue). Representation of the point cloud for a simulation case with curved boundary, where the fluid points are deleted if they move closer than the value $r_{\min}h$ to avoid clustering, which gives rise to a void region between the wall points and the fluid points.

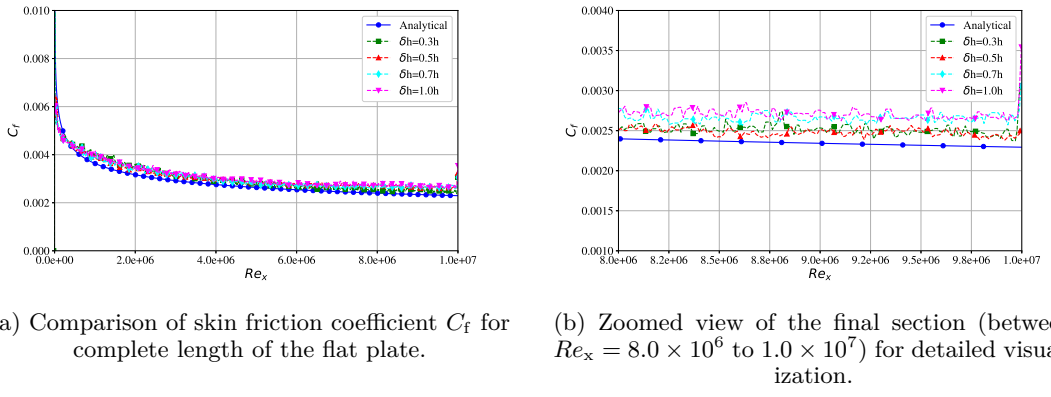


Figure 12. Comparison of skin friction coefficient C_f with various selection heights δh using the nearest band neighbor method. The plots show selection heights of $\delta h = 0.3h$ (green), $\delta h = 0.5h$ (red), $\delta h = 0.7h$ (cyan), $\delta h = 1h$ (magenta) against the analytical expression (blue). The zoomed view reveals that $\delta h = 0.5h$ provides the best match with the analytical solution, followed by $\delta h = 0.3h$, while $\delta h = 0.7h$ and $\delta h = 1h$ show slight deviations due to the selection of a larger number of points for applying the wall function.

Skin friction results for different δ values are shown in Figure 12. All these cases generally follow the analytical trend, but there are some fluctuations caused by random point positions and varying wall-normal distances. If we focus on the well-developed region near the end of the plate, $\delta h = 0.3h$ and $\delta h = 0.5h$ agree best with the analytical values, while $\delta h = 1.0h$ is less accurate because it includes points far from the wall corresponding to higher y^+ values, which increases errors and computational cost. Based on these results, we use $\delta h = 0.5h$ for further NBN simulations.

With NBN and $\delta h = 0.5h$, we compared three turbulence models: Spalart–Allmaras (SA), standard $k-\varepsilon$, and $k-\omega$ (Wilcox, 2006), see Figure 13. With SA a Neumann wall boundary is set, and the wall-adjacent eddy viscosity ν_t is modified based on the wall function. SA exhibits larger fluctuations in C_f near the initial length of the plate, due to sensitivity to wall function coupling under Neumann treatment. The $k-\varepsilon$ model is more diffusive and underpredicts C_f , whereas $k-\omega$ tends to slightly overpredict C_f once the boundary layer is developed. Velocity profiles at $x = 1.0$ m and $y = 0.5$ m, non-dimensionalized by the friction velocity u_τ (i.e.,

$u^+ = u/u_\tau$), show that wall shear stress prediction accuracy directly influences the velocity profile (see Figure 14).

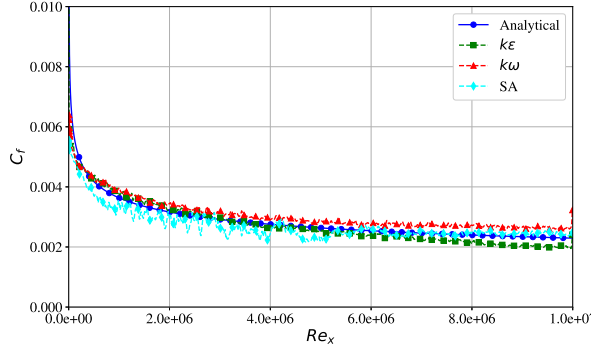


Figure 13. Comparison of Skin Friction Coefficient C_f for Various Turbulence Models (SA (Green line), $k - \varepsilon$ (Red line), and $k - \omega$ (Cyan line)) against the analytical expression using the nearest-band neighbor method in turbulent flow over a flat plate. The figure indicates that $k - \omega$ provides superior accuracy near the wall compared to $k - \varepsilon$ and SA models.

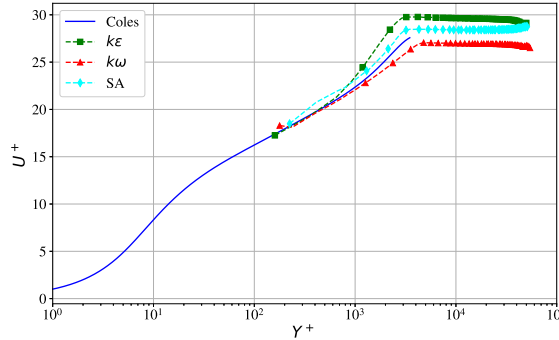


Figure 14. Comparison of velocity profile at the wall normal direction with respect to U^+ , y^+ for various turbulence models (SA (Green line), $k - \varepsilon$ (Red line), and $k - \omega$ (Cyan line)) against the analytical expression with Cole's theory [12] (blue) using the nearest-band neighbor method in turbulent flow over a flat plate. The turbulence model SA shows a better fit with the velocity profile compared to $k - \omega$, which underpredicts the velocities close to bulk flow, and $k - \varepsilon$ overpredicts the velocities at the bulk flow.

4.2.3. Shifted-boundary (SB) Method Analysis Since point positions move with the flow velocity in a Lagrangian sense, and points are added or removed during the simulation to maintain uniformity, y^+ at wall-adjacent points cannot be fixed, which motivates the adoption of the shifted boundary method (SB) to get more consistent wall-adjacent point distances. In this approach, the wall function is applied at virtually shifted points, all located at a fixed distance αh from the wall. We also examine the same evaluation carried out with the NBN method, also with SB, such as wall-function effects, selection height sensitivity, and turbulence model behavior. The simulation and flow parameters are set similar to those of the NBN method, but with a resolution $h = 0.005$ m due to the possibility of having the shifted points $\alpha h = 0.1h$ lower than that with the NBN method and still having a similar y^+ range. The diffusion operator uses a momentum height βh (see Section 3.3). These shifted points guarantee controlled wall function application regardless of point motion.

Initial comparisons between standard and Launder–Spalding wall functions employ shifted height $\alpha h = 0.1h$ and momentum thickness $\beta h = 2.0\alpha h$ with the $k - \omega$ turbulence model. Both methods yield comparable results due to the simple flat plate configuration lacking high turbulent fluctuations or pressure gradients, see Figure 15. The Launder–Spalding formulation is selected for subsequent analyses.

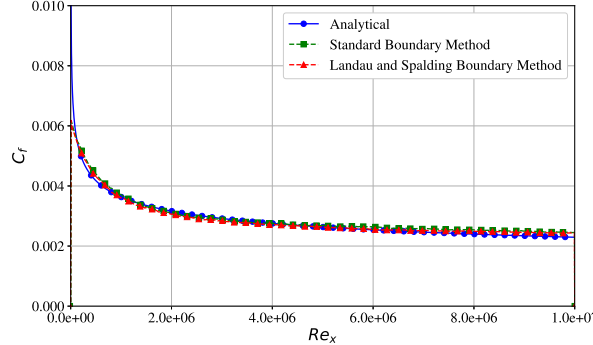


Figure 15. Comparison of Skin Friction Coefficient C_f for shifted boundary method with Standard wall-function method (green) and Launder–Spalding method (red) against the analytical solution (blue) (von Karman, Theodore). The simulation is carried out using the $k - \omega$ turbulence model with resolution h of 0.005, shifted height $\alpha h = 0.1h$, and momentum thickness of $\beta h = 0.2h$.

As the wall functions are selected, the next step is to study the effect of the virtual shift height αh . For this, shifted heights of $\alpha h = 0.05h$, $0.1h$, $0.2h$, and $0.4h$ are tested, with $\beta h = 2\alpha h$ (see Figure 16). At $\alpha h = 0.05h$, the shifted and momentum points lie in regions with very few neighbors, which biases the wall function and leads to underprediction of C_f . For $\alpha h = 0.1h$ and $0.2h$, the shifted point is located within the region where no other points are present due to the point deletion criteria $r_{min}h$, and βh sits at the interface with the interior, ensuring accurate results. When $\alpha h = 0.4h$, the shifted point is too far from the wall, even resulting in interior points situated between the boundary and shifted points to which the wall function is not applied. This leads to inconsistency in how the wall functions are imposed, leading to large errors similar to those of the CN method. The range $0.1h$ to $0.2h$ (with $\beta h = 2\alpha h$) yields the best performance. For all further SB cases, $\alpha h = 0.1h$ is used.

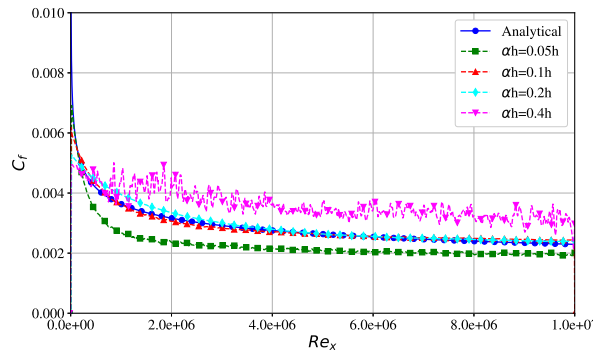


Figure 16. Comparison of Skin Friction Coefficient C_f with different shifted height αh with shifted boundary method for shifted height of $\alpha h = 0.05h$ (green), $\alpha h = 0.1h$ (red), $\alpha h = 0.2h$ (cyan), $\alpha h = 0.4h$ (pink). The comparison shows that the shifted height of $\alpha h = 0.1h$ to $0.2h$ give the best match to the analytical solution, with $0.2h$ and $0.1h$ giving a larger deviation with respect to the analytical expression.

The next step is to study the effect of βh by fixing the shifted height αh . With $\alpha h = 0.1h$ fixed, the momentum height βh values of $1.5\alpha h$, $2\alpha h$, and $3\alpha h$ are evaluated for diffusion operator accuracy, see Figure 17. The configuration with $\beta h = 2\alpha h$ gives the most accurate results, as it provides even spacing between the wall, shifted point, and momentum stencil point. Having βh too small (too close to the wall) or too large (too deep into the interior) introduces asymmetry and small errors. Setting $\beta h \geq r_{\min}h$ and maintaining near-equidistant spacing ensures optimal accuracy.

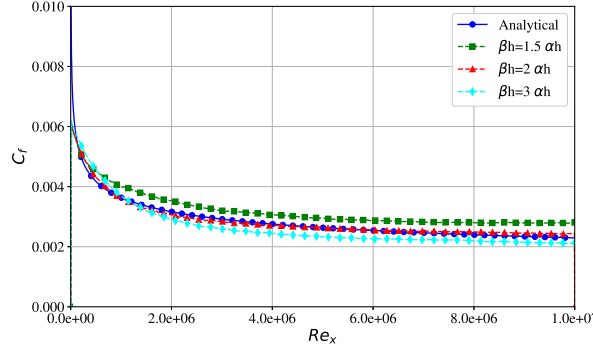


Figure 17. Comparison of Skin Friction Coefficient C_f for momentum height $\beta h = 1.5\alpha h$ (green), $\beta h = 2.0\alpha h$ (red), $\beta h = 3\alpha h$ (cyan) with shifted-boundary method. The sC_f comparison shows equidistant spacing between αh and βh gives better results compared to the values.

With $\alpha h = 0.1h$ and $\beta h = 0.2h$, all three turbulence models (SA, $k-\varepsilon$, $k-\omega$) deliver nearly overlapping C_f curves (see Figure 18) with minor variation towards the end of the flat plate. With respect to the velocity profiles, the turbulence models agree with the analytical solution (see Figure 19) with variation of the velocity away from the flat plate towards the bulk flow. Compared to NBN, SB maintains fixed wall-normal sampling and achieves lower y^+ values for the same mesh(free) coarseness, strengthening both accuracy and robustness. Thus, this method also enables coarser grids while keeping y^+ within the required range.

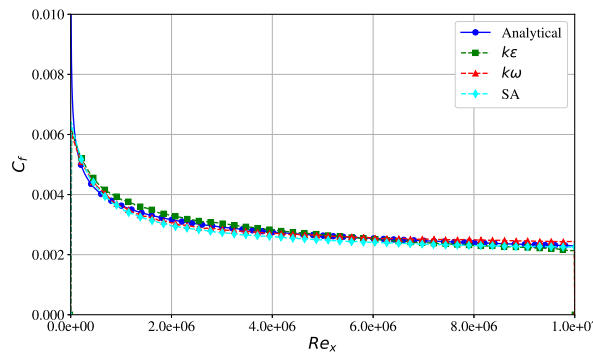


Figure 18. Comparison of Skin Friction Coefficient C_f for various turbulence models (SA (Green line), $k - \varepsilon$ (Red line), and $k - \omega$ (Cyan line)) against the analytical expression (blue) using the shifted boundary method in turbulent flow Over a flat plate: similar trend can be observed between all the turbulence models and match well with respect to analytical expression with slight variation at the end of the flat plate.

4.2.4. Computation cost and performance analysis While selecting the boundary treatment method, in addition to accuracy, the computation cost required for each method is also

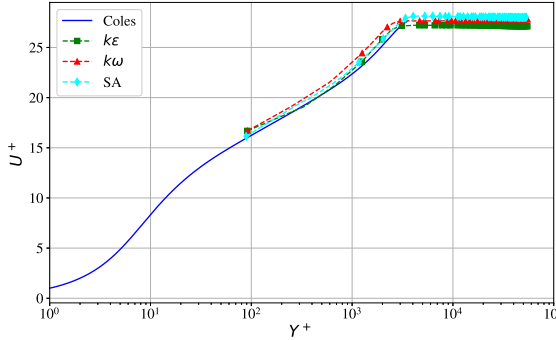


Figure 19. Comparison of velocity profile at the wall normal direction with respect to U^+ , y^+ for various turbulence models (SA (Green line), $k - \varepsilon$ (Red line), and $k - \omega$ (Cyan line)) against Cole's theory [12] (blue) using the shifted boundary method in turbulent flow over a flat plate. The results show a similar profile with minor variation towards the bulk flow region.

crucial. We compare the computation cost for each method to carry out the different steps in the algorithm and the total cost. The CN method is excluded due to poor performance. We compare the remaining NBN and SB methods to reveal a trade-off between the computational overhead required for the boundary treatment and the cost savings gained from a coarser point cloud resolution.

The Shifted Boundary Method (SB) successfully achieves a comparable near-wall resolution (i.e., the same y^+ value) to the Nearest Band Neighbor Method (NBN), even when employing a resolution 30% larger (coarser) than that required for the NBN. Crucially, this yields the same skin friction C_f results comparable to the NBN, particularly for the flat plate benchmark case.

Whereas for NBN, achieving this identical y^+ value with increased resolution causes the point cloud density to increase in all three directions, leading to an overall increase of approximately 50% to 60% in the total number of simulation points. With a 50% increase in the number of points, the total computation time increases by roughly 50%, raising the total time per time step from 92.5 seconds to approximately 152.6 seconds for the NBN method. This demonstrates a clear net advantage for the SB in large simulation cases where minimizing the total number of points is critical for efficiency.

The computational cost of the NBN and SB boundary treatment operations was compared based on a simulation setup comprising approximately $\approx 5 \times 10^5$ points. All simulations were carried out on 48 processors using MPI parallelization, and all reported CPU times are averaged over one thousand time steps to ensure reliable performance data.

The NBN has two primary steps contributing to its computational cost: (i) Selection of interior neighbors next to the wall based on the distance δh . (ii) Computation of the wall stress using the wall function for all selected points for both the momentum equation and turbulence equation. The time taken for these two setups are shown in the table I

Table I. Computational time for nearest-band neighbor (NBN) method

| Operation | Time Taken (seconds) |
|-------------------------------------|----------------------|
| Nearest neighbors search (Step 1) | 0.07 |
| Applying the wall function (Step 2) | 0.05 |

The main computational costs for the SB are associated with the geometry and derivative calculations at the boundary. The first is the operation of the virtual shift of the boundary points to a distance ah in the normal direction. The second is the computation of differential

operators with respect to the normal and tangential directions. The differential operator split computation is required for the momentum equation and may also be necessary for turbulence equations (e.g., the kinetic energy (k) equation, especially when using the Launder–Spalding wall function). The computation time taken for each of these steps is shown in Table II

Table II. Computational time for shifted boundary (SB) method

| Operation | Time Taken (seconds) |
|--|----------------------|
| Virtual shift of points | 0.04 |
| Computing normal and tangential components (Momentum Equation) | 1.30 |
| Computing gradients/Source Terms (k Equation) | 0.90 |
| Computing wall stresses (Turbulence Equation) | 0.07 |

The total time required for the SB boundary treatment operations is significantly higher than the NBN, with the NBN being approximately 19.8 times faster for the localized boundary treatment steps alone.

However, the complete time taken to compute all primary flow equations (momentum, turbulence, and pressure) for all points is approximately 92.5 seconds per time step. When benchmarked against this total simulation time, the additional cost of the SB is comparatively low. Therefore, the SB offers a significant net advantage by preventing the large $\sim 50\%$ increase in total simulation time that results from the finer point cloud resolution required to make the NBN comparable in near-wall resolution.

4.3. Flow around a NACA12 wing

The next simulation test case considers the flow around a curved boundary. For this, we chose a 3D flow simulation around a wing with a NACA 0012 airfoil profile. The wing is placed in a rectangular channel, with a chord length of 1 m and a width of 1 m. The channel itself is 10 m long and 5 m high, with the channel width matching the wing's width. The wing is positioned 2 m from the inflow and 2.5 m above the bottom wall, as shown in Figure 20. The side, top, and bottom walls of the channel have slip boundary conditions.

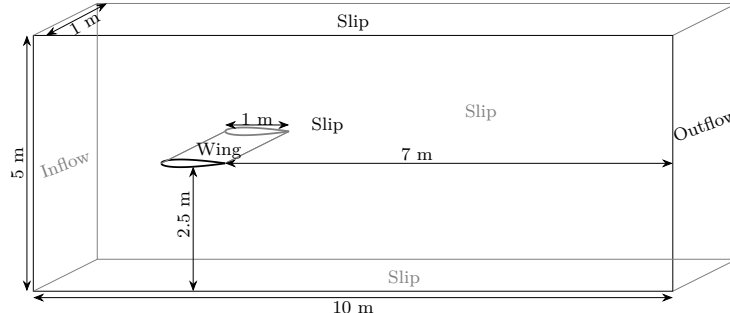


Figure 20. Flow over a 3D wing with NACA-0012 profile, illustrating the dimensions of the rectangular channel and the placement of the wing. Includes inlet conditions such as specified velocity and pressure gradient, along with slip and no-slip boundary condition sections.

For the simulation, air is used as the fluid, with a density of $\rho = 1 \text{ kg m}^{-3}$ and a kinematic viscosity (ν) of $\nu = 8.544 \times 10^{-6} \text{ m}^2 \text{ s}^{-1}$. The inflow velocity (V_∞) is set to 51.2 m s^{-1} with a constant velocity and a 0° angle of attack, resulting in a Mach number of approximately $M = 0.15$ and a Reynolds number of around $\text{Re} = 3 \times 10^6$ on the wing's chord. The flow is considered purely incompressible.

The resolution for the mesh-free discretization is chosen such that it is smaller closer to the wing and increases with distance from the wing as shown from the Figure 21. We tested two

boundary treatment methods: nearest band neighbor (NBN) and shifted boundary method (SB). The optimized parameters from the flat plate case were used. For the NBN method, the resolution is $h = 0.003\text{ m}$, with a selection height of $\delta h = 0.4h$. For the SB, we have $h = 0.0035\text{ m}$, with a shifted height of $\alpha h = 0.1h$ and a momentum height of $\beta h = 0.2h$.

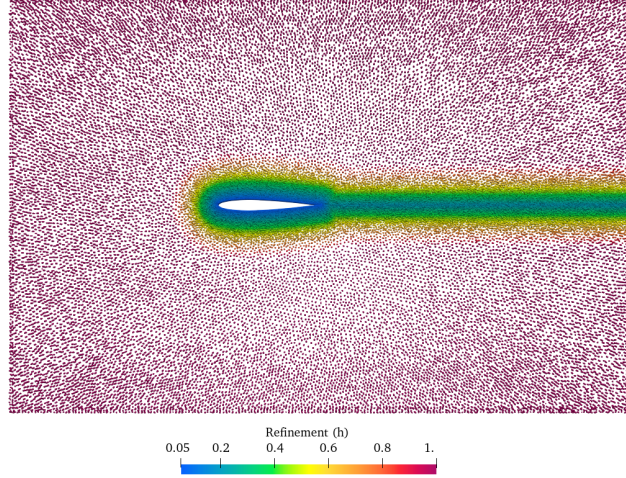


Figure 21. Refinement strategy for the flow around a NACA-0012 profile. The normalized refinement size h varies from 0.05 (blue) near the airfoil surface to 1.0 (magenta) at the far-field boundary. All h values are normalized, and this visualization serves to illustrate the gradient variation across the domain.

The Launder–Spalding wall function, with the $k - \omega$ standard turbulence model, is used for the wall function methods. Both boundary treatment methods are compared to study their effects on the drag coefficient, the lift coefficient, and skin friction. Initially, we examined the variation of skin friction values and compared them with results from a finite volume method-based CFD code called CFL3D.

When comparing the two boundary treatment methods, we observed that the shifted boundary method agrees well at the leading edge up to a chord length of 0.35 m, after which it slightly underpredicts, resulting in a local minimum. In contrast, the nearest band neighbor method initially underpredicts the skin friction coefficients but gets closer to the CFL3D reference values after a chord length of 0.35 m. Beyond this point, the values are slightly underpredicted but remain closer to the reference values, as shown in Figure 22. This phenomenon is observed with different turbulence models and variations of αh and βh , suggesting that the effects arise from parameters other than the boundary treatment method.

Next, we compared the lift and drag coefficients at a 0° angle of attack. Compared to experimental results [24] at $\text{Re} \approx 3 \times 10^6$, the lift coefficient is typically $C_L = 0$ for a symmetric wing profile at a 0° angle of attack, and the drag coefficient ranges from $C_D = 0.006$ to $C_D = 0.009$. The lift and drag coefficients obtained from NBN and SB methods are shown in Table III. We observed that the lift coefficients are slightly off from the experimental results for both methods. However, the drag coefficient for the SB is within the suggested range from the experimental results, while the NBN method deviates slightly with a lower value of $C_D = 0.0049$.

Table III. Aerodynamic Coefficients for NACA 0012 Airfoil at 0° Angle of Attack

| Boundary Treatment | Lift Coefficient (C_L) | Drag Coefficient (C_D) |
|-----------------------|----------------------------|----------------------------|
| Shifted-boundary | 0.0102 | 0.0072 |
| Nearest-band neighbor | -0.0227 | 0.0049 |

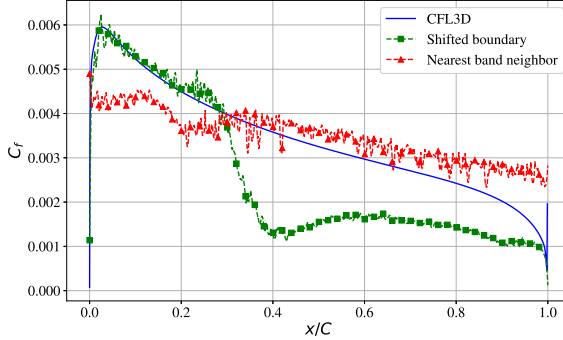


Figure 22. Comparison of Skin Friction Coefficient C_f along the length of the wing with both shifted-boundary (green) and nearest-band neighbor method (red) with resolution of h of 0.0035m and 0.003m respectively. The simulation is carried out using the $k - \omega$ turbulence model.

The reason for the mismatch in skin friction values requires further investigation. Parameter studies show that the effects persist, and this needs to be studied further.

5. CONCLUSION

In this paper, we address the challenges associated with implementing wall treatment methods in meshfree collocation methods. We propose two novel strategies for handling wall functions in Lagrangian meshfree for URANS simulations. These wall treatment techniques have been developed, implemented, and systematically evaluated to establish a foundation for applying wall functions to high Reynolds number turbulent flow problems.

The comparative analysis reveals clear performance differences between the three approaches. The closest neighbor method is straightforward to implement, but it suffers from fundamental limitations due to non-uniform point selection. This leads to gaps in wall function coverage and consequently causes numerical instabilities. It consistently overpredicts skin friction coefficients and produces large instantaneous fluctuations, making it unsuitable for treating wall functions.

The nearest band neighbor (NBN) method shows substantial improvements over the closest neighbor approach. In this method, all interior points within a specified distance δh from the wall are selected to apply the wall function. This ensures uniform coverage and more consistent wall function application. Numerical results show that the selection height of $\delta h = 0.5h$ provides the best balance between accuracy and computational efficiency. Both wall function strategies (standard and Launder-Spalding) produced similar results, so we adopted the Launder-Spalding method for its superior transport properties. However, this method requires dynamic point identification at each time step due to the Lagrangian nature of the meshfree framework. Furthermore, the varying distance of the interior points from the boundary induces fluctuations that propagate to the bulk flow.

The shifted boundary (SB) method overcomes the drawbacks of the nearest band neighbor and offers additional advantages. In this method, boundary points are virtually shifted by a fixed distance αh in the boundary normal direction from the wall towards the interior of the domain. This eliminates the need for dynamic point selection while maintaining consistent wall-normal distances throughout the domain. Our numerical results show that the shifted height $\alpha h = 0.1h$ and momentum thickness $\beta h = 0.2h$ provided the best results. Because the shift distance αh in the SB is smaller than the selection distance δh of the NBN method, similar y^+ can be achieved even with coarser point clouds with the shifted boundary method. Due

to the coarser resolution, the SB method results in approximately 50% fewer total simulation points than the NBN method allows, thus significantly reducing computational cost.

Regarding the turbulence model, the Spalart–Allmaras model provides better accuracy across all wall treatment methods, particularly in the near-wall region, followed by the $k-\omega$ and $k-\varepsilon$ models. The shifted boundary method shows better consistency across all three turbulence models, with nearly overlapping results for both skin friction coefficients and velocity profiles.

Validation against established benchmark cases confirms that both NBN and SB boundary treatment methods perform well with 3D flat plate boundary layers and the 3D wing with NACA 0012 profile. The shifted boundary method achieves excellent agreement with analytical solutions for flat plate flows and reasonable agreement with reference CFD data for the NACA airfoil case. However, with the NACA airfoil case, the shifted boundary method underpredicts the skin friction coefficients, showing variations in the results that need to be investigated further.

Regarding the computational cost, the analysis reveals that the shifted boundary method requires more expensive boundary treatment operations (approximately 20 times costlier than NBN for boundary operations alone). However, the overall computational advantage from coarser point count resolutions actually results in significant net time savings for large-scale simulations.

This work establishes meshfree methods as viable alternatives to traditional mesh-based approaches for high-Reynolds-number turbulent flow applications. The wall treatment methods developed, particularly the shifted boundary approach, provide the robustness and accuracy needed for high Reynolds number flows while preserving the advantages of meshfree collocation methods, such as natural adaptivity, simplified preprocessing for complex geometries, and suitability for moving boundary problems. Future research should be investigate the cause for the underprediction of the skin friction in curved boundaries, like in the NACA wing profile, with the shifted boundary method. Furthermore, to extend the wall-function treatment to more complex scenarios, such as adverse pressure gradients, flow separation cases need to be investigated.

REFERENCES

- [1] M. Antuono et al. “Smoothed particle hydrodynamics method from a large eddy simulation perspective. Generalization to a quasi-Lagrangian model”. en. In: *Physics of Fluids* 33.1 (2021), p. 015102.
- [2] Jun Arai, Seiichi Koshizuka, and Koji Murozono. “Large eddy simulation and a simple wall model for turbulent flow calculation by a particle method”. en. In: *International Journal for Numerical Methods in Fluids* 71.6 (2013), pp. 772–787.
- [3] B. Aupoix and P.R. Spalart. “Extensions of the Spalart–Allmaras turbulence model to account for wall roughness”. en. In: *International Journal of Heat and Fluid Flow* 24.4 (2003), pp. 454–462.
- [4] Tingting Bao et al. “Smoothed particle hydrodynamics with $k - \varepsilon$ closure for simulating wall-bounded turbulent flows at medium and high Reynolds numbers”. en. In: *Physics of Fluids* 35.8 (2023), p. 085114.
- [5] T. Belytschko et al. “Meshless methods: An overview and recent developments”. en. In: *Computer Methods in Applied Mechanics and Engineering* 139.1-4 (1996), pp. 3–47.
- [6] J. Boussinesq. *Essai sur la théorie des eaux courantes*. Mémoires présentés par divers savants à l’Académie des sciences de l’Institut national de France. Impr. nationale, 1877.
- [7] Jonas Bredberg. *On the Wall Boundary Condition for Turbulence Models*. 2000.
- [8] David L. Brown, Ricardo Cortez, and Michael L. Minion. “Accurate Projection Methods for the Incompressible Navier–Stokes Equations”. In: *Journal of Computational Physics* 168.2 (2001), pp. 464–499.
- [9] Jiun-Shyan Chen, Michael Hillman, and Sheng-Wei Chi. “Meshfree Methods: Progress Made after 20 Years”. en. In: *Journal of Engineering Mechanics* 143.4 (2017), p. 04017001.

[10] Kuei-Yuan Chien. "Predictions of Channel and Boundary-Layer Flows with a Low-Reynolds-Number Turbulence Model". en. In: AIAA Journal 20.1 (1982), pp. 33–38.

[11] Alexandre Joel Chorin. "Numerical solution of the Navier-Stokes equations". In: Mathematics of computation 22.104 (1968), pp. 745–762.

[12] Donald Coles. "The law of the wake in the turbulent boundary layer". en. In: Journal of Fluid Mechanics 1.2 (1956), pp. 191–226.

[13] T.J. Craft et al. "Progress in the generalization of wall-function treatments". en. In: International Journal of Heat and Fluid Flow 23.2 (2002). Publisher: Elsevier BV, pp. 148–160.

[14] Christian Drumm et al. "Finite pointset method for simulation of the liquid - liquid flow field in an extractor". In: Computers & Chemical Engineering 32.12 (2008), pp. 2946–2957.

[15] Fraunhofer Society. MESHFREE. <https://www.meshfree.eu>.

[16] Hitoshi Gotoh and Abbas Khayyer. "On the state-of-the-art of particle methods for coastal and ocean engineering". en. In: Coastal Engineering Journal 60.1 (2018), pp. 79–103.

[17] Paul S. Granville. "Drag and Turbulent Boundary Layer of Flat Plates at Low Reynolds Numbers". en. In: Journal of Ship Research 21.01 (1977), pp. 30–39.

[18] Tomas Halada et al. "An Overview of Meshfree Collocation Methods". In: arXiv preprint arXiv:2509.20056 (2025).

[19] X.Y. Hu and N.A. Adams. "A multi-phase SPH method for macroscopic and mesoscopic flows". en. In: Journal of Computational Physics 213.2 (2006), pp. 844–861.

[20] Anthony Jefferies et al. "Finite Pointset Method for the Simulation of a Vehicle Travelling Through a Body of Water". In: Meshfree Methods for Partial Differential Equations VII. Ed. by Michael Griebel and Alexander Marc Schweitzer. Cham: Springer International Publishing, 2015, pp. 205–221.

[21] B.A. Kader. "Temperature and concentration profiles in fully turbulent boundary layers". en. In: International Journal of Heat and Mass Transfer 24.9 (1981), pp. 1541–1544.

[22] Georgi Kalitzin et al. "Near-wall behavior of RANS turbulence models and implications for wall functions". en. In: Journal of Computational Physics 204.1 (2005), pp. 265–291.

[23] Joerg Kuhnert. "Meshfree numerical scheme for time dependent problems in fluid and continuum mechanics". In: Advances in PDE Modeling and Computation. Ed. by S. Sundar. New Delhi: Anne Books, 2014, pp. 119–136.

[24] C.L. Ladson et al. Effects of Independent Variation of Mach and Reynolds Numbers on the Low-speed Aerodynamic Characteristics of the NACA 0012 Airfoil Section. NASA technical memorandum. National Aeronautics, Space Administration, Scientific, and Technical Information Division, 1988.

[25] B.E. Launder and D.B. Spalding. "The numerical computation of turbulent flows". en. In: Computer Methods in Applied Mechanics and Engineering 3.2 (1974), pp. 269–289.

[26] T. Liszka and J. Orkisz. "The finite difference method at arbitrary irregular grids and its application in applied mechanics". en. In: Computers & Structures 11.1-2 (1980), pp. 83–95.

[27] Gui-Rong Liu and Y. T. Gu. An introduction to Meshfree methods and their programming. eng. Dordrecht: Springer, 2010.

[28] Rainald Löhner and Eugenio Oñate. "An advancing front point generation technique". en. In: Communications in Numerical Methods in Engineering 14.12 (1998), pp. 1097–1108.

[29] Hong-Guan Lyu et al. "Towards SPH simulations of cavitating flows with an EoSB cavitation model". en. In: Acta Mechanica Sinica 39.2 (2023), p. 722158.

[30] I. Marusic et al. "Wall-bounded turbulent flows at high Reynolds numbers: Recent advances and key issues". en. In: Physics of Fluids 22.6 (2010), p. 065103.

[31] Takeharu Matsuda and Satoshi Ii. A least-squares meshfree method for the incompressible Navier-Stokes equations: A satisfactory solenoidal velocity field via a staggered-variable arrangement. Version Number: 1. 2025.

- [32] A. Mayrhofer et al. “DNS and LES of 3-D wall-bounded turbulence using Smoothed Particle Hydrodynamics”. en. In: *Computers & Fluids* 115 (2015), pp. 86–97.
- [33] F. R. Menter. “Two-equation eddy-viscosity turbulence models for engineering applications”. en. In: *AIAA Journal* 32.8 (1994), pp. 1598–1605.
- [34] Domenico Davide Meringolo et al. “Large eddy simulation within the smoothed particle hydrodynamics: Applications to multiphase flows”. en. In: *Physics of Fluids* 35.6 (2023), p. 063312.
- [35] Isabel Michel et al. “A meshfree generalized finite difference method for solution mining processes”. In: *Computational Particle Mechanics* 8.3 (2021), pp. 561–574.
- [36] J.J. Monaghan. “Smoothed Particle Hydrodynamics and Its Diverse Applications”. en. In: *Annual Review of Fluid Mechanics* 44.1 (2012), pp. 323–346.
- [37] M. Naghian, M. Lashkarbolok, and E. Jabbari. “Numerical Simulation of Turbulent Flows Using a Least Squares Based Meshless Method”. en. In: *International Journal of Civil Engineering* 15.1 (2017), pp. 77–87.
- [38] Akihiko Nakayama, Xin Yan Lye, and Khai Ching Ng. “Wall-layer boundary condition method for laminar and turbulent flows in weakly-compressible SPH”. en. In: *European Journal of Mechanics - B/Fluids* 95 (2022), pp. 276–288.
- [39] Vinh Phu Nguyen et al. “Meshless methods: A review and computer implementation aspects”. en. In: *Mathematics and Computers in Simulation* 79.3 (2008), pp. 763–813.
- [40] Vivek G. Patel and Nikunj V. Rachchh. “Meshless method – Review on recent developments”. en. In: *Materials Today: Proceedings* 26 (2020), pp. 1598–1603.
- [41] L. Prandtl. “7. Bericht über Untersuchungen zur ausgebildeten Turbulenz”. en. In: *ZAMM - Journal of Applied Mathematics and Mechanics / Zeitschrift für Angewandte Mathematik und Mechanik* 5.2 (1925), pp. 136–139.
- [42] H. Reichardt. “Vollständige Darstellung der turbulenten Geschwindigkeitsverteilung in glatten Leitungen”. en. In: *ZAMM - Journal of Applied Mathematics and Mechanics / Zeitschrift für Angewandte Mathematik und Mechanik* 31.7 (1951), pp. 208–219.
- [43] Herrmann Schlichting and Klaus Gersten. *Boundary-Layer Theory*. en. Berlin, Heidelberg: Springer Berlin Heidelberg, 2000.
- [44] P. Spalart and S. Allmaras. “A one-equation turbulence model for aerodynamic flows”. en. In: 30th Aerospace Sciences Meeting and Exhibit. Reno,NV,U.S.A.: American Institute of Aeronautics and Astronautics, 1992.
- [45] Stein K.F. Stoter et al. “Nitsche’s method as a variational multiscale formulation and a resulting boundary layer fine-scale model”. en. In: *Computer Methods in Applied Mechanics and Engineering* 382 (2021), p. 113878.
- [46] Pratik Suchde, Thibault Jacquemin, and Oleg Davydov. “Point Cloud Generation for Meshfree Methods: An Overview”. en. In: *Archives of Computational Methods in Engineering* 30.2 (2023), pp. 889–915.
- [47] Pratik Suchde, Thibault Jacquemin, and Oleg Davydov. “Point cloud generation for meshfree methods: an overview”. In: *Archives of Computational Methods in Engineering* 30.2 (2023), pp. 889–915.
- [48] Pratik Suchde and Joerg Kuhnert. “A meshfree generalized finite difference method for surface PDEs”. In: *Computers & Mathematics with Applications* 78.8 (2019), pp. 2789–2805.
- [49] Pratik Suchde and Jörg Kuhnert. “A fully Lagrangian meshfree framework for PDEs on evolving surfaces”. en. In: *Journal of Computational Physics* 395 (2019), pp. 38–59.
- [50] Pratik Suchde and Jörg Kuhnert. “Point Cloud Movement For Fully Lagrangian Meshfree Methods”. In: *Journal of Computational and Applied Mathematics* 340 (2018), pp. 89–100.
- [51] Pratik Suchde and Jörg Kuhnert. “Point cloud movement for fully Lagrangian meshfree methods”. en. In: *Journal of Computational and Applied Mathematics* 340 (2018), pp. 89–100.

- [52] Pratik Suchde, Jörg Kuhnert, and Sudarshan Tiwari. “On meshfree GFDM solvers for the incompressible Navier–Stokes equations”. en. In: Computers & Fluids 165 (2018), pp. 1–12.
- [53] M. M. M. El Telbany and A. J. Reynolds. “Velocity distributions in plane turbulent channel flows”. en. In: Journal of Fluid Mechanics 100.01 (1980), p. 1.
- [54] Henk Tennekes and John L. Lumley. A First Course in Turbulence. en. The MIT Press, 1972.
- [55] D. Violeau and R. Issa. “Numerical modelling of complex turbulent free-surface flows with the SPH method: an overview”. en. In: International Journal for Numerical Methods in Fluids 53.2 (2007), pp. 277–304.
- [56] David C. Wilcox. “Formulation of the k-w Turbulence Model Revisited”. en. In: AIAA Journal 46.11 (2008), pp. 2823–2838.
- [57] Chi Zhang et al. “An efficient and generalized solid boundary condition for SPH: Applications to multi-phase flow and fluid–structure interaction”. en. In: European Journal of Mechanics - B/Fluids 94 (2022), pp. 276–292.